

Inverse cascades and resonant triads in rotating and stratified turbulence

D. Oks¹, P.D. Mininni^{1,2}, R. Marino³, and A. Pouquet^{2,4}

¹ *Universidad de Buenos Aires, Facultad de Ciencias Exactas y Naturales, Departamento de Física, & IFIBA, CONICET, Ciudad Universitaria, Buenos Aires 1428, Argentina.*

² *NCAR, P.O. Box 3000, Boulder, Colorado 80307-3000, USA.*

³ *Laboratoire de Mécanique des Fluides et d'Acoustique, CNRS, École Centrale de Lyon, Université de Lyon, 69134 Écully, France.*

⁴ *Laboratory for Atmospheric and Space Physics, CU, Boulder, Colorado 80309-256, USA.*

(Dated: March 6, 2023)

Kraichnan seminal ideas on inverse cascades yielded new tools to study common phenomena in geophysical turbulent flows. In the atmosphere and the oceans, rotation and stratification result in a flow that can be approximated as two-dimensional at very large scales, but which requires considering three-dimensional effects to fully describe turbulent transport processes and non-linear phenomena. Motions can thus be classified into two classes: fast modes consisting of inertia-gravity waves, and slow quasi-geostrophic modes for which the Coriolis force and horizontal pressure gradients are close to balance. In this paper we review previous results on the strength of the inverse cascade in rotating and stratified flows, and then present new results on the effect of varying the strength of rotation and stratification (measured by the ratio N/f of the Brunt-Väisälä frequency to the Coriolis frequency) on the amplitude of the waves and on the flow quasi-geostrophic behavior. We show that the inverse cascade is more efficient in the range of N/f for which resonant triads do not exist, $1/2 \leq N/f \leq 2$. We then use the spatio-temporal spectrum, and characterization of the flow temporal and spatial scales, to show that in this range slow modes dominate the dynamics, while the strength of the waves (and their relevance in the flow dynamics) is weaker.

I. INTRODUCTION

Kraichnan landmark paper on inverse cascades in two-dimensional (2D) turbulence [1] has been the stepping stone for a substantial fraction of the research carried out in geophysical turbulence in the last 50 years. Besides introducing the concept of a range of scales in which energy can flow with constant flux from smaller to larger scales, it presented a vision of turbulent flows which was vastly different to that of the disorganized flow often associated with three-dimensional (3D) Kolmogorov turbulence. The inverse energy cascade allows interpretation of phenomena in geophysical and astrophysical flows that is at odds with the picture of turbulence of Richardson and Kolmogorov. However, as Montgomery and Kraichnan wrote in the concluding remarks of their famous review [2], “*great caution must be used when interpreting phenomena of the real world in terms of asymptotic solutions of approximate statistical treatments of idealised theory.*” But Kraichnan and Montgomery went beyond this warning, also suggesting that the idealized 2D system may find its largest relevance in providing a language for discussion of common phenomena observed in geophysics.

Indeed, the language and tools developed in the study of inverse cascades have found applications in a large variety of systems. The occurrence of inverse cascades can be explained using statistical mechanics in inviscid truncated systems [1, 2]: when the system has two or more quadratic conserved quantities, the solutions are not just the thermal equilibrium between all modes, which leads to the accumulation of the conserved quantities at small scales. Instead, other solutions can develop involving the accumulation of one of the conserved quantities at large

scales. Moreover, this behavior is preserved in forced and dissipative cases. To alleviate the concerns of the authors of Ref. [2], the increase in computing power and the improvement in experimental methods and *in situ* measurements allowed researchers to confirm these predictions, and to consider flows in geometries or in the presence of external forces that permitted the study of turbulence in setups that are closer to the real world. The predictions for the two-dimensional hydrodynamic case have been verified in experiments and in high-resolution numerical simulations [3–8]. Inverse cascades are by now known to also take place in conducting fluids and plasmas [9–14], with important consequences in space physics and astrophysics [15]. In atmospheric sciences, the inverse cascade plays a fundamental role in the study of predictability [16–19]. And also in atmospheric sciences, an inverse cascade of energy is known to take place in the quasi-geostrophic (QG) equations [20–23], which describe the large-scale dynamics of atmospheric and oceanic flows. In this case, the joint conservation of energy and of potential enstrophy is responsible for the inverse cascade which has been also verified numerically [24].

The atmosphere is a rotating and stratified flow with very large aspect ratio. While typical horizontal scales can be of the order of a thousand kilometers, in the vertical direction the typical height of the troposphere is ≈ 10 km. These features result in a flow that can be approximated as a 2D flow at very large scales, but which requires considering 3D rotating and stratified flows to describe in detail small scale turbulent transport processes and non-linear phenomena. Compared with homogeneous and isotropic turbulence (HIT), buoyancy forces associated with density gradients and the inertial Coriolis force associated with the rotation of the Earth pro-

vide the necessary restitutive forces to allow excitation of dispersive waves. Thus, geophysical flows are often in a highly turbulent state comprised of non-linearly interacting eddies and waves. These motions can be classified into two classes: on the one hand, 3D modes consisting of inertia-gravity waves evolving on a fast time scale, and on the other hand, large-scale QG modes which evolve in a slow time scale, and for which the Coriolis force and horizontal pressure gradients are close to balance.

The influence of rotation and stratification in the dynamics of the atmosphere and the oceans varies depending on the scale studied. At the largest geophysical scales, both rotation and stratification are significant, and the QG regime is expected to be dominant. In the range $\mathcal{O}(800\text{--}2500)$ km it has been observed that the atmospheric energy spectrum scales as $E(k) \sim k^{-3}$ [25], a power law consistent with the classical QG theory of Charney [20]. As smaller scales are considered, the influence of these restitutive forces on the system dynamics decreases. Following the classical view, as the scale of interest is decreased, the importance of rotation decreases faster than that of stratification. At atmospheric mesoscales (horizontal scales of $\mathcal{O}(1\text{--}100)$ km), and in the submesoscale ocean ($\mathcal{O}(10)$ m to $\mathcal{O}(10)$ km), motions are characterized by a strong stratification with moderate rotation (with Rossby number $Ro \approx 1$, see [26]). At these scales, the energy spectrum scales approximately as $E(k) \sim k^{-5/3}$ [25, 27, 28]. While in the atmosphere the origin of this scaling is still unclear [29], in the ocean some evidence of an inverse cascade of energy has been found (see, e.g., [30] for a study of an inverse energy cascade from observations in the South Pacific, and [31] for numerical simulations of an inverse energy cascade in the North Atlantic). In the atmosphere it was suggested that this scaling can be the result of a 2D inverse cascade fed by convective instabilities [21, 32]. The possible coexistence (without significant distortions) of a direct cascade range with $E(k) \sim k^{-3}$ fed by large scale instabilities, and of an inverse cascade range with $E(k) \sim k^{-5/3}$ fed by instabilities at small scales, was predicted before in [33, 34]. However, a $E(k) \sim k^{-5/3}$ scaling can also be observed in the direct cascade range of rotating and stratified turbulence, and recent atmospheric observations also seem to point to a direct cascade process [35, 36].

In fact, there is growing evidence from numerical simulations that there is a large variety of turbulent regimes depending on whether geostrophic balance is broken or not, on whether QG modes dominate over wave modes or not, and on how energy is introduced in the system [37–43]. A recent re-analysis of oceanic data, and theoretical developments in wave turbulence theory, also indicate that there is a variety of regimes depending on whether waves or eddies dominate [44]. Finally, the interactions between eddies, winds and waves in the atmosphere and the oceans have dynamical consequences for the transport and mixing of momentum, CO_2 , and heat [45, 46]. Thus, it is very important to understand the interactions between all modes in the system, and to properly charac-

terize the different regimes that exist in parameter space.

In the particular case of the inverse cascade range, and when considering both rotation and stratification, several phenomena can compete resulting in different regimes. In the presence of large scale forcing (see, e.g., [35, 47–52]) inverse cascades cannot be observed. With small scale forcing conclusions are somewhat contradictory, and differ depending on whether weak rotation, weak stratification, or rotation and stratification of comparable strength are considered. When rotation and stratification are of comparable strength, inverse cascades were reported [53–55], and were associated with the dynamics of QG modes in the system. In purely rotating systems energy can cascade both to the large and to the small scales [56, 57], with the inverse cascade being associated with the 2D modes of the system. For this case different scaling laws in the inverse cascade range were also reported depending on how the flow is stirred [41]. Finally, for negligible or no rotation, although an increase of energy and of the integral vertical length scale was reported in simulations [37, 38], Waite and Bartello [39, 40] conclude against the presence of an inverse cascade using an argument based on statistical mechanics, similar to the one used by Kraichnan to predict the inverse cascade in 2D flows. More recently [58] showed, using a detailed analysis of anisotropic fluxes, that the growth of vertical length scales in this system is the result of highly anisotropic energy transfers associated with the formation of *vertically sheared horizontal winds* (VSHW, see [37]).

The transition between these inverse cascade regimes was believed to vary monotonically with N/f , a ratio measuring the strength of stratification to rotation, where N is the Brunt-Väisälä frequency and f the Coriolis frequency. Indeed, theoretical arguments suggest that the ratio of energy in horizontal, vertical, and QG modes is governed by this ratio [59] (see also [53, 54] for numerical studies), and several studies showed that for fixed rotation, increasing the stratification slows down the inverse cascade (at least for $N/f \leq 1$). However, in a recent study [60] it was shown that the inverse cascade growth rate is non-monotonic in N/f , with a behavior for $N/f < 2$ different from the one found for $N/f \geq 2$ for which the result of monotonic decrease of the inverse cascade rate with increasing N/f is recovered. In this study it was also found that a moderate level of stratification (in the sense that $1/2 \leq N/f \leq 2$) produces a faster growth of energy at large scale than in the purely rotating case. Although linear theories predicted a different behavior [59], the non-monotonicity on N/f could be expected from the theory of non-linear resonant interactions in wave turbulence [40, 61–65].

The relevance (or not) of the wave modes in these flows can be understood from results in the theory of resonant waves. With sufficient rotation and stratification, nonlinear interactions between triads of wave modes are expected to become the predominant mechanism of energy transfer. Resonant wave theory predicts that given three modes with wave vectors \mathbf{k} , \mathbf{p} , and \mathbf{q} , these can

interact and transfer energy between themselves if the wave vectors form a triangle with $\mathbf{k} = \mathbf{p} + \mathbf{q}$, and if the modes are also resonant, i.e., if their frequencies satisfy $\omega(\mathbf{k}) = \omega(\mathbf{p}) + \omega(\mathbf{q})$ [61, 63]. While this theory explains the development of anisotropy and the tendency towards two-dimensionalization of some flows (necessary for the development of inverse cascades), it fails to explain how energy reaches the slow modes which seem to be the dominant modes in the inverse cascade dynamics [63]. Interestingly, the relevance of these interactions is non-monotonic with increasing rotation and stratification. In the case of rotating and stratified flows, there is a range of parameters $1/2 \leq N/f \leq 2$ for which all resonances are cancelled out. Outside this region, the first resonant triads that arise with $N/f < 1/2$ tend to two-dimensionalize the flow, forming vertical structures in the shape of columns, while the first resonant triads arising for $N/f > 2$ tend to unidimensionalize the flow, forming structures in the shape of pancakes. Thus inverse cascades can be expected to be stronger in the former case. In between, when resonant interactions are not present and QG modes can be expected to be dominant, Charney [20] argues that turbulence should be isotropic in the rescaled vertical coordinate $(N/f)z$, implying that the quotient between horizontal and vertical scales should grow linearly with N/f . The non-monotonic behavior of resonant triads with N/f can therefore be expected to play a role in the development of inverse cascades.

In this paper we first review previous results on the strength of the inverse cascade in rotating and stratified flows, and then present new results on the effect of varying the strength of rotation and stratification (measured by the ratio N/f) on the amplitude of the waves and on the QG behavior of the flow. We use the spatio-temporal spectrum, and characterization of the flow temporal and spatial scales, to show that in the range $1/2 \leq N/f \leq 2$ QG modes dominate the dynamics, while the strength of the waves is weaker. The structure of the remaining of the paper is as follows. Section II introduces the Boussinesq approximation, discusses the role of linear solutions of the equations and of the resonant triads, and shows that resonant triads do not exist for $1/2 \leq N/f \leq 2$. Then, in Sec. III we review previous results on inverse cascades in rotating and stratified flows. We consider the purely rotating case, the purely stably stratified case, and parametric studies of rotating and stratified flows as a function of N/f . Sections IV and V then present new results. In Sec. IV we present a parametric study using several simulations at moderate spatial resolution, and show that simulations in the range $1/2 \leq N/f \leq 2$ are compatible with some predictions from QG theory. Then, in Sec. V we use the spatio-temporal spectrum to quantify the strength of the waves and of QG modes, and explicitly show that waves are less relevant in the same range of N/f . Finally, in Sec. VI we present the conclusions.

II. THE BOUSSINESQ APPROXIMATION

A. The equations

The dynamics of a stably stratified incompressible fluid subjected to background rotation can be described, under the Boussinesq approximation, by the momentum equation for the velocity \mathbf{u} , and an equation for the temperature fluctuations θ ,

$$\partial_t \mathbf{u} + \boldsymbol{\omega} \times \mathbf{u} + 2\boldsymbol{\Omega} \times \mathbf{u} = -\nabla \mathcal{P} - N\theta \hat{z} + \mathbf{f} + \nu \nabla^2 \mathbf{u}, \quad (1)$$

$$\frac{\partial \theta}{\partial t} + \mathbf{u} \cdot \nabla \theta = N\mathbf{u} \cdot \hat{z} + \kappa \nabla^2 \theta, \quad (2)$$

together with the incompressibility condition,

$$\nabla \cdot \mathbf{u} = 0. \quad (3)$$

Here gravity points in the \hat{z} direction, and for simplicity we will also consider the rotation axis in the same direction, so that $\boldsymbol{\Omega} = \Omega \hat{z}$ where Ω is the rotation frequency and $f = 2\Omega$ the Coriolis frequency. In Eq. (1) N is the Brunt-Väisälä frequency, \mathbf{f} is an external mechanical forcing, \mathcal{P} is the total pressure per unit of mass (including the centrifugal acceleration and the background hydrostatic pressure), and ν is the kinematic viscosity. In Eq. (2) κ is the thermal diffusivity (in the following equal to the kinematic viscosity, $\kappa = \nu$, so the Prandtl number is $\text{Pm} = 1$).

Three dimensionless numbers play an important role to characterize the different regimes in the system. These are the Reynolds, Rossby, and Froude numbers

$$\text{Re} = \frac{UL}{\nu}, \quad \text{Ro} = \frac{U}{fL}, \quad \text{Fr} = \frac{U}{NL} \quad (4)$$

where U is the r.m.s. velocity and L the flow integral scale. While the former measures the ratio of inertial to viscous accelerations in the flow, the two latter are respectively inverse measures of the relevance of rotation and of stratification. The ratio N/f can be written in terms of these numbers as $N/f = \text{Ro}/\text{Fr}$. Other dimensionless numbers are known to play important roles (e.g., the buoyancy Reynolds number $\text{Rb} = \text{Re}\text{Fr}^2$ [45, 47, 50, 66], or the scales at which rotation [67, 68] or stratification [51, 69] become negligible).

When the Reynolds number is large enough the system is in a turbulent state. But even at very large Reynolds numbers, for Fr and Ro small enough, waves are present that affect the turbulent scaling and transport. Thus this system of equations has been extensively studied in numerical simulations as a way to gain a better understanding of atmospheric turbulence in a simplified set up. As mentioned in the introduction, in the atmospheric mesoscales (where the stratification dominates above the rotation, but the dominant regime is quasi-geostrophic and not dominated by inertia-gravity waves), a spectrum of energy compatible with the power law $E(k) \sim k^{-3}$ has

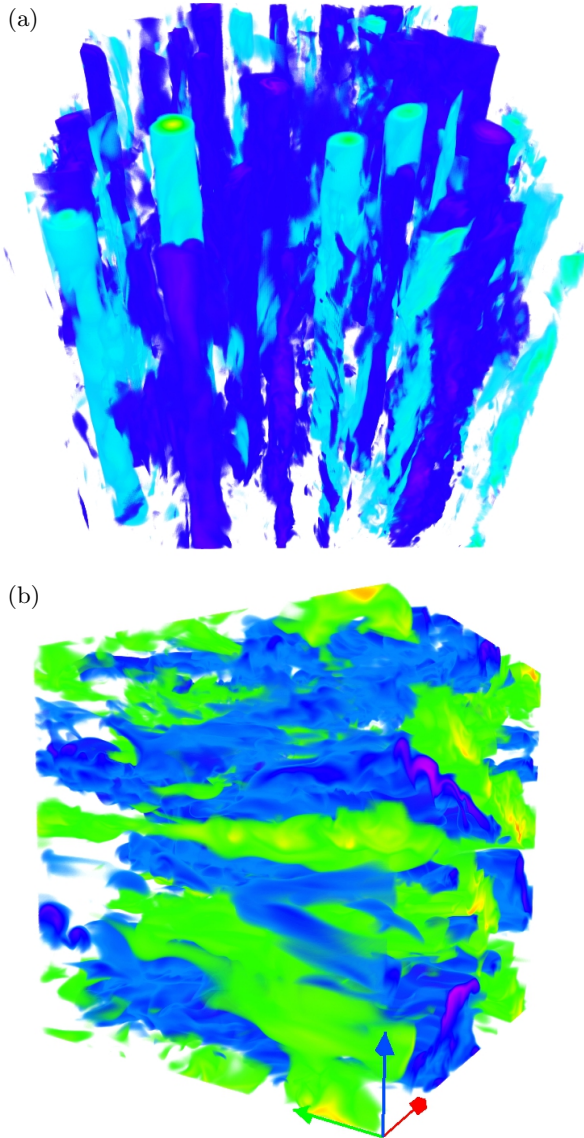


FIG. 1: (*Color online*) (a) Vertical velocity in a 1536^3 simulation of rotating turbulence [57]. Note the presence of column-like structures. (b) Temperature fluctuations in a 1024^3 simulation of rotating and stratified turbulence with weak rotation [60]. Note the formation of slanted layers, with an angle proportional to the ratio N/f . In the purely stratified case, the layers are horizontal.

been reported. However, a spectrum $E(k) \sim k^{-5/3}$ has also been observed (see, e.g., [70]), and numerical simulations of Eqs. (1)-(3) have generated results consistent with this power law in the presence of instabilities and small-scale overturning [35, 71]. However, when overturning is suppressed by dissipation, the spectrum in the simulations becomes steeper. The asymptotic dynamics of this system in the limit of strongly rotating flows generates column-like structures [61], while in the limit of strongly stratified vortical motions it seems to consist of quasi-horizontal fluid layers decoupled between them-

selves [72] (see Fig. 1). While in the rotating case the direct cascade spectrum of Eqs. (1)-(3) seems to scale as $E(k) \sim k^{-2}$ [25, 57, 61, 65], Billant and Chomaz [73] argue that in the purely stratified case the vertical characteristic scale L_z scales as U/N , thus suggesting that the vertical energy spectrum should follow a power law $E(k_z) \sim N^2 k_z^{-3}$. This behavior was observed in numerical simulations [35, 43, 69], where it was also observed that in the purely stratified case the parallel spectrum $E(k_z)$ is flat for wave numbers smaller than $k_z \sim N/U$ [39, 56, 69]. As the parallel spectrum dominates over the perpendicular when stratification is sufficiently strong, the isotropic spectrum also follows a law $E(k) \sim k^{-3}$ in the purely stratified case. In the following sections we introduce a decomposition of the flow into slow and fast modes, and the argument of resonant triads, that allow interpretation of some of these results in the direct cascade range, to later consider the case of the inverse cascade.

B. Linear modes

In the inviscid limit and in the absence of external forces ($\nu = \kappa = \mathbf{f} = 0$), the Boussinesq equations conserve the potential vorticity

$$\frac{D}{Dt} (\boldsymbol{\omega}_a \cdot \nabla \theta) = 0, \quad (5)$$

where $\boldsymbol{\omega}_a$ is the absolute (total) vorticity in the laboratory frame, $\boldsymbol{\omega}_a = \boldsymbol{\omega} + 2\boldsymbol{\Omega}$. When rotation and the Brunt-Väisälä frequencies are homogeneous, except for a multiplying prefactor and a constant term, the potential vorticity can be written as

$$P.V. = f \frac{\partial \theta}{\partial z} - N \omega_z + \boldsymbol{\omega} \cdot \nabla \theta. \quad (6)$$

The conservation of potential vorticity imposes strong constraints on the flow. As a result, solutions to the Boussinesq equations are often decomposed into two groups of modes: inertia-gravity waves with non-zero frequency and zero potential vorticity (also called “fast” modes), and modes with zero frequency and non-zero potential vorticity (also called “slow” modes). By replacing solutions

$$(\mathbf{u}, \theta) = \boldsymbol{\psi}(\mathbf{k}) e^{i(\mathbf{k} \cdot \mathbf{x} + \omega t)}, \quad (7)$$

in the linearized Boussinesq equations, three modes per wave vector \mathbf{k} can be identified. The two modes with non-zero frequency have dispersion relation [26]

$$\omega(\mathbf{k}) = \pm \frac{\sqrt{f^2 k_{\parallel}^2 + N^2 k_{\perp}^2}}{k}, \quad (8)$$

where the directions parallel and perpendicular are taken with respect to the direction of gravity and of the rotation

axis, i.e., $k_{\parallel} = k_z$, $k_{\perp} = (k_x^2 + k_y^2)^{1/2}$, and $k = |\mathbf{k}|$. The group velocity for these modes is

$$\mathbf{c} = \frac{f^2 - N^2}{\sigma k^4} [\mathbf{k} \times (k_{\parallel} \hat{\mathbf{z}} \times \mathbf{k})], \quad (9)$$

and for $f = N$ it can be expected that the role of the waves in the flow dynamics should be less relevant. Also, note that for $f = 0$ (the purely stratified case) Eq. (8) reduces to the dispersion relation of internal gravity waves (with the modes with $k_{\perp} = 0$ corresponding to the VSHW [37], which have zero frequency and are thus “slow”). And in the case with $N = 0$ (purely rotating flow), the dispersion relation reduces to that of inertial waves (with the slow modes corresponding to 2D modes with $k_{\parallel} = 0$).

In the non-linear case, the fields in Fourier space can be expanded in terms of these three modes [26, 63, 74–78],

$$(\mathbf{u}_{\mathbf{k}}, \theta_{\mathbf{k}}) = a^{+}(\mathbf{k}, t) \psi^{+}(\mathbf{k}) e^{i\omega t} + a^{-}(\mathbf{k}, t) \psi^{-}(\mathbf{k}) e^{-i\omega t} + a^0(\mathbf{k}, t) \psi^0(\mathbf{k}), \quad (10)$$

where $a^{(\alpha)}(\mathbf{k}, t)$ (with $\alpha = +, -, 0$ labeling the three modes) are slowly evolving amplitudes.

C. Resonant triads

Fourier transforming the Boussinesq equation, and using the decomposition in Eq. (10), the following equation is obtained [63, 74, 75]

$$\begin{aligned} \frac{da_{\mathbf{k}}^{(\alpha)}}{dt} &= \sum_{\mathbf{k}=\mathbf{p}+\mathbf{q}} C_{\mathbf{kpq}}^{\alpha\beta\gamma} a_{\mathbf{p}}^{(\beta)} a_{\mathbf{q}}^{(\gamma)} e^{i(\sigma_{\mathbf{p}}^{(\beta)} + \sigma_{\mathbf{q}}^{(\gamma)} - \sigma_{\mathbf{k}}^{(\alpha)})} \\ &+ F_{\mathbf{k}}^{(\alpha)} - D_{\mathbf{k}}^{(\alpha)}, \end{aligned} \quad (11)$$

where $C_{\mathbf{kpq}}^{\alpha\beta\gamma}$ is a coupling coefficient between modes, $F_{\mathbf{k}}^{(\alpha)}$ is the energy injection at wavenumber \mathbf{k} , and $D_{\mathbf{k}}^{(\alpha)}$ is the dissipation. The first term on the r.h.s. of this equation corresponds to the non-linear triadic interactions. As nonlinearities in the Boussinesq equations are quadratic, modes are coupled with triads that can exchange energy between themselves while conserving the total energy. The convolution theorem (when the quadratic terms are Fourier transformed) imposes the well known triadic condition

$$\mathbf{k} = \mathbf{p} + \mathbf{q}. \quad (12)$$

But the presence of waves imposes an extra condition. Integrating Eq. (11) in one period of the waves, the first term on the r.h.s. of the equation vanishes except when

$$\sigma_{\mathbf{k}}^{(\alpha)} = \sigma_{\mathbf{p}}^{(\beta)} + \sigma_{\mathbf{q}}^{(\gamma)}, \quad (13)$$

which is the so-called resonant triad condition, and selects only the triads with constructive interference between the non-linearly interacting waves.

Waleffe describes the triadic interactions exhaustively for homogeneous turbulence in [62], and the resonant triadic interactions for rapidly rotating flows in [63], where he presents an argument for the two-dimensionalization of rotating flows. His “instability assumption” states that the statistical direction of the energy transfer is determined by the stability of the corresponding elemental triadic interaction. In practice, this results in a preferential transfer of energy towards the modes with zero frequency, although wave turbulence theories can not explain how energy ultimately reaches these modes [79, 80]. In spite of this, the argument is successful in explaining how anisotropy develops. As mentioned in Sec. II B, for purely rotating flows Eq. (8) reduces to $\omega(\mathbf{k}) = \pm f k_{\parallel}/k$, which is the dispersion relation of inertial waves. Energy is then transferred preferentially towards modes with $k_{\parallel} \approx 0$, which correspond to the 2D modes, and if the energy can reach those modes it can be expected to suffer an inverse cascade towards large scales. In purely stratified flows Eq. (8) reduces to $\omega(\mathbf{k}) = \pm N k_{\perp}/k$ (internal gravity waves), and energy then is transferred preferentially towards modes with $k_{\perp} \approx 0$, i.e., to modes with vertical shear. In the former case this explains the formation of structures with small vertical gradients (columns, see Fig. 1), while in the latter case it explains the formation of pancake-like structures (see also Fig. 1).

D. Characteristic time scales

In wave turbulence the presence of multiple time scales does not allow for direct estimation of scaling laws in the inertial range as is often done in Kolmogorov theory of turbulence. While in HIT there is only one time scale in the inertial range (the eddy turnover time), in the presence of waves this time scale coexists with the period of the waves, precluding the construction of a unique time scale on dimensional grounds. While in weak wave turbulence regimes this problem can be circumvented (see, e.g., [81]), in the strong turbulent case the problem persists. Interestingly, one of the first advances towards the construction of phenomenological theories for this kind of systems was also done by Kraichnan, who put forward a theory for the interaction of eddies and Alfvén waves in magnetohydrodynamic turbulence [82].

Thus, it is important to identify the different time scales relevant in our problem. The decomposition introduced in Sec. II B is useful to this end. The first time scale will naturally be proportional to the wave period

$$\tau_w(\mathbf{k}) = \frac{C_w}{\omega(\mathbf{k})} = \frac{C_w k}{\sqrt{f^2 k_{\parallel}^2 + N^2 k_{\perp}^2}}, \quad (14)$$

where C_w is a dimensionless constant of $\mathcal{O}(1)$ which can be obtained directly from the auto-correlation function of the Fourier modes of the velocity and temperature fields (see [83]).

From Eq. (11) it is to be expected that the fastest time dominates the flow dynamics and the energy transfer. However, although for small enough Ro and Fr the waves are expected to be fast, the period of the waves is not homogeneous in Fourier space as it depends on \mathbf{k} . Thus, different regions of Fourier space can be dominated by different time scales depending on what mode is the fastest. The period of the waves must then be compared with the eddy turnover time

$$\tau_{nl}(k) = \frac{C_{nl}}{k\sqrt{kE(k)}}, \quad (15)$$

where C_{nl} is another dimensionless constant of $\mathcal{O}(1)$. In principle τ_{nl} depends on the direction in Fourier space, i.e., $\tau_{nl}(\mathbf{k})$, since the energy spectrum in these systems is anisotropic. But for simplicity we will use here the isotropic energy spectrum $E(k)$ to estimate the non-linear time.

The last relevant time scale is that of the sweeping of the small eddies by the large scale flow, which becomes the dominant Eulerian decorrelation mechanism as soon as its characteristic time scale becomes the fastest of the three (Kraichnan also played an important role in highlighting the relevance of this time scale [84]). The time to sweep an eddy of size $\sim 1/k$ by a large scale flow with amplitude U is simply

$$\tau_{sw}(k) = \frac{C_{sw}}{Uk}, \quad (16)$$

where C_{sw} is another dimensionless constant of $\mathcal{O}(1)$ that can be determined from the data. These time scales will be very important in the following sections.

Using combinations of these time scales, phenomenological theories for the direct cascade spectrum can be also constructed, following the ideas of Kraichnan [82]. These phenomenological arguments yield spectra compatible with the scaling laws $\sim k^{-2}$ and $\sim k^{-3}$ discussed in the introduction and in Sec. II A, for solutions of Eqs. (1)-(3) depending on the strength of rotation and stratification considered. For more details see [73, 85–87].

E. Non-resonant range

It can be shown that in the range $1/2 \leq N/f \leq 2$ there are no resonant triadic interactions, and therefore all triadic interactions must be non-resonant [37]. As discussed in Sec. II C, non-linear interaction of inertia-gravity waves require that the interacting modes \mathbf{k} , \mathbf{p} , and \mathbf{q} form a triangle, and that the sum of their frequencies give constructive interference. If $N = f$, it is then trivial to see from Eq. (8) that $\omega(\mathbf{k}) = \pm N$ for all \mathbf{k} , and then

$$\sigma(\mathbf{p}) + \sigma(\mathbf{q}) - \sigma(\mathbf{k}) = \pm N, \pm 2N, \text{ or } \pm 3N. \quad (17)$$

Therefore, the sum of the three frequencies cannot be zero and the condition given by Eq. (13) cannot be fulfilled.

In the most general case, Eq. (8) implies that

$$\min\{|\sigma(\mathbf{k})|\} = \min\{N, f\}, \quad (18)$$

$$\max\{|\sigma(\mathbf{k})|\} = \max\{N, f\}. \quad (19)$$

Assuming without loss of generality $\sigma(\mathbf{k}), \sigma(\mathbf{p}), \sigma(\mathbf{q}) > 0$, to satisfy Eq. (13) we need $2 \min\{N, f\} < \max\{N, f\}$. When $\max\{N, f\} = N$ we then need $N/f > 2$. When $\max\{N, f\} = f$, then $N/f < 1/2$. In these cases there are triads which can satisfy the resonant condition. However, in the range

$$\frac{1}{2} \leq \frac{N}{f} \leq 2, \quad (20)$$

there is no triad that can be resonant.

It is now clear that this range separates to regimes with different behavior. It is expected that outside this range, but in its vicinity, very few resonant triads should be available. Thus, resonant triads should play a more relevant role for $N/f \ll 1/2$ or $N/f \gg 2$. For $N/f < 1/2$ the first resonant triads that arise consist of a vertical mode $(0, 0, k_{\parallel})$ and two quasi-horizontal modes \mathbf{p}, \mathbf{q} with $p_{\perp} = q_{\perp} \gg |k_{\parallel}|, |p_{\parallel}|, |q_{\parallel}|$. Waleffe's instability assumption then suggests that energy should go from the vertical mode to the perpendicular (slow) modes. Similarly, for $N/f > 2$, the first resonant triads consist of a horizontal mode and two quasi-vertical modes. In this case, the transfer should be expected to occur from the horizontal modes to the quasi-vertical (slow) modes. As with the arguments in Sec. II C, these arguments suggest that the first resonant triads that arise when $N/f < 1/2$ tend to bi-dimensionalize the flow, whereas the first resonant triads that arise when $N/f > 2$ tend to unidimensionalize the flow (see Fig. 1).

F. Quasi-geostrophic equation

Simulations with $1/2 \leq N/f \leq 2$ show that QG modes dominate the dynamics at scales larger than the forced scales [56], in agreement with the theoretical prediction that resonant triads are not available in this region of parameter space. This can be used to derive a reduced system of equations. Although the QG approximation is often derived in the limit of very small Froude number and moderate rotation (of interest in atmospheric sciences), Smith and Waleffe [37, 56] showed that the QG equations can also be obtained for moderate values of N/f , which can be of interest for oceanographic applications.

If only modes with zero frequency are excited, in the inviscid and unforced case Eq. (11) can be written as

$$\frac{da_{\mathbf{k}}^0}{dt} = \sum_{\mathbf{k}=\mathbf{p}+\mathbf{q}} C_{\mathbf{k}\mathbf{p}\mathbf{q}} a_{\mathbf{p}}^0 a_{\mathbf{q}}^0, \quad (21)$$

where

$$C_{\mathbf{k}\mathbf{p}\mathbf{q}} \equiv C_{\mathbf{k}\mathbf{p}\mathbf{q}}^{000} = \frac{iN(\mathbf{p} \times \mathbf{q}) \cdot \hat{\mathbf{z}}}{kpq\omega_{\mathbf{k}}\omega_{\mathbf{p}}\omega_{\mathbf{q}}} (\omega_{\mathbf{q}}^2 q^2 - \omega_{\mathbf{p}}^2 p^2). \quad (22)$$

The triadic condition in Eq. (12) implies that $(\mathbf{p} \times \mathbf{q}) \cdot \hat{z} = (\mathbf{q} \times \mathbf{k}) \cdot \hat{z} = (\mathbf{k} \times \mathbf{p}) \cdot \hat{z}$, that is, that the $C_{\mathbf{k}\mathbf{p}\mathbf{q}}$ coupling coefficients are cyclic permutations of the wave vectors multiplied by $\omega_{\mathbf{q}}^2 q^2 - \omega_{\mathbf{p}}^2 p^2$. It then follows that

$$C_{\mathbf{k}\mathbf{p}\mathbf{q}} + C_{\mathbf{p}\mathbf{q}\mathbf{k}} + C_{\mathbf{q}\mathbf{p}\mathbf{k}} = 0, \quad (23)$$

$$\omega_{\mathbf{k}}^2 k^2 C_{\mathbf{k}\mathbf{p}\mathbf{q}} + \omega_{\mathbf{p}}^2 p^2 C_{\mathbf{p}\mathbf{q}\mathbf{k}} + \omega_{\mathbf{q}}^2 q^2 C_{\mathbf{q}\mathbf{p}\mathbf{k}} = 0, \quad (24)$$

which convey two conservation laws as discussed below.

Taking $\phi_{\mathbf{k}} = -Na_{\mathbf{k}}^0/(k\omega_{\mathbf{k}})$, and Fourier transforming Eq. (21) into real space, we obtain

$$\left(\frac{\partial}{\partial t} + \mathbf{v} \cdot \nabla\right) \left(\nabla_{\perp}^2 + \frac{f^2}{N^2} \frac{\partial^2}{\partial z^2}\right) \phi(\mathbf{x}, t) = 0, \quad (25)$$

where $\nabla_{\perp}^2 = \partial_x^2 + \partial_y^2$, $\mathbf{v} = \hat{z} \times \nabla \phi$, and $\theta = -(f/N)\partial_z \psi$. This is the quasi-geostrophic equation, which conserves two quadratic invariants: the total energy

$$E = \frac{1}{2} \left\langle |\nabla_{\perp} \psi|^2 + \frac{f^2}{N^2} \left(\frac{\partial \psi}{\partial z}\right)^2 \right\rangle, \quad (26)$$

with $\nabla_{\perp} = \partial_x \hat{x} + \partial_y \hat{y}$, and the potential enstrophy

$$F = \frac{1}{2} \left\langle \left(\nabla_{\perp}^2 \psi + \frac{f^2}{N^2} \frac{\partial^2 \psi}{\partial z^2}\right)^2 \right\rangle. \quad (27)$$

As in the 2D case studied by Kraichnan [1], the existence of two invariants in this case also allows for the development of an inverse cascade of energy [20, 21, 24].

III. INVERSE CASCADES

To discuss previous results in inverse cascades, and to analyze the new results in this paper, we will use isotropic and anisotropic spectra and fluxes. We thus begin by defining the isotropic kinetic energy spectrum, which is computed in numerical simulations as

$$E_V(k) = \frac{1}{2} \sum_{k \leq |\mathbf{k}| < k+1} |\mathbf{u}(\mathbf{k})|^2, \quad (28)$$

i.e., as the energy in spherical shells of width $\Delta k = 1$ in Fourier space. An equivalent definition is obtained for the potential energy spectrum $E_P(k)$ replacing $|\mathbf{u}(\mathbf{k})|^2$ by $|\theta(\mathbf{k})|^2$, and the total energy spectrum is then simply constructed as $E(k) = E_V(k) + E_P(k)$. The kinetic energy spectrum can be further decomposed into the kinetic energy in horizontal fluctuations and in vertical fluctuations, $E_V(k) = E_{\perp}(k) + E_z(k)$, where $E_{\perp}(k)$ is the energy in the x and y components of the velocity field, and $E_z(k)$ is the energy in u_z .

As the flows we consider are anisotropic, it is useful to define the axisymmetric kinetic energy spectrum

$$e_v(k_{\perp}, k_{\parallel}) = \frac{1}{2} \sum_{\substack{k_{\perp} \leq |\mathbf{k} \times \hat{z}| < k_{\perp} + 1 \\ k_{\parallel} \leq k_z < k_{\parallel} + 1}} |\mathbf{u}(\mathbf{k})|^2, \quad (29)$$

The axisymmetric energy spectrum in Eq. (29) is such that the total energy in 2D modes is $E_{2D} = \sum_{k_{\perp}} e(k_{\perp}, k_{\parallel} = 0)$. As a result, we will refer to $e(k_{\perp}, k_{\parallel} = 0)$ as the energy spectrum of the 2D modes. Note in Eqs. (28) and (29) we use sums as we are considering the discrete Fourier transform for a triple 2π -periodic spatial domain. In the most general case these sums are replaced by integrals.

To quantify energy scaling in the parallel and perpendicular directions, reduced perpendicular and parallel spectra can then be defined from the axisymmetric energy spectrum as:

$$E(k_{\perp}) = \sum_{k_{\parallel}} e(k_{\perp}, k_{\parallel}), \quad (30)$$

and

$$E(k_{\parallel}) = \sum_{k_{\perp}} e(k_{\perp}, k_{\parallel}). \quad (31)$$

Identification of inverse cascades requires not only the study of the growth of energy in these spectra for small wave numbers, but also quantification of negative flux of energy in a range of wave numbers. To this end we can define anisotropic transfer functions associated with each energy spectra $E(k)$, $E(k_{\perp})$, and $E(k_{\parallel})$ respectively as

$$T(k) = - \sum_{k \leq |\mathbf{k}| < k+1} t(\mathbf{k}), \quad (32)$$

$$T(k_{\perp}) = - \sum_{k_{\perp} \leq |\mathbf{k} \times \hat{z}| < k_{\perp} + 1} t(\mathbf{k}), \quad (33)$$

$$T(k_{\parallel}) = - \sum_{k_{\parallel} \leq k_z < k_{\parallel} + 1} t(\mathbf{k}), \quad (34)$$

where $t(\mathbf{k}) = \mathbf{u}^*(\mathbf{k}) \cdot (\widehat{\mathbf{u} \cdot \nabla \mathbf{u}}) + \theta^*(\mathbf{k}) (\widehat{\mathbf{u} \cdot \nabla \theta}) + c.c.$, where $*$ and $c.c.$ denotes complex conjugate, and the superscript $\widehat{}$ denotes the Fourier transform. From these functions anisotropic fluxes are then defined as follows:

$$\Pi(k) = - \sum_{k'=0}^k T(k'), \quad (35)$$

$$\Pi(k_{\perp}) = - \sum_{k'_{\perp}=0}^{k_{\perp}} T(k'_{\perp}), \quad (36)$$

$$\Pi(k_{\parallel}) = - \sum_{k'_{\parallel}=0}^{k_{\parallel}} T(k'_{\parallel}). \quad (37)$$

These fluxes measure energy per unit of time that goes in Fourier space respectively across spheres with radius k , across cylinders with radius k_{\perp} , and across planes with height $k_{\parallel} = \text{constant}$.

A. Rotating case

In the purely rotating case with moderate Rossby numbers, the preferential transfer of energy towards 2D modes results in the development of an inverse cascade which shares some similarities with the inverse cascade originally proposed by Kraichnan. By now evidence of this inverse cascade has been found in numerical simulations in finite domains [41] and in experiments [88]. There is still a controversy of whether this inverse cascade can take place in infinite domains and for very small Rossby numbers, for more details see, e.g., Ref. [89].

An interesting property of the inverse cascade of energy in this case is that changes in the forcing function or in the dominant time scale can generate large differences in the scaling of the energy spectrum (see [41]). In particular, the anisotropy of the forcing seems to play an important role in setting the shape of the inverse cascade energy spectrum. As an illustration, Fig. 2 shows the reduced perpendicular spectrum and the horizontal kinetic energy spectrum of 2D modes for two simulations of rotating turbulence forced at small scales.

The two simulations have $Re \approx 400$ and $Ro = 0.045$. The difference between these two simulations is in the isotropy (or anisotropy) of the forcing function. While in both cases a random forcing is used, in one case energy is injected isotropically in all modes in the spherical shell with $k = k_F \approx 40$, while in the other energy is injected mostly in the modes (in the same spherical shell) that are close to the k_\perp plane (i.e., preferentially into modes with small k_\parallel , or the 2D modes). A detailed analysis of anisotropic fluxes in [41] shows that while in the former case this results in a transfer of energy from the 3D modes to the 2D modes which then drive the inverse cascade, in the latter case the energy that is fed directly into the 2D modes undergoes an inverse cascade and then feeds the 3D modes once the energy accumulates at the largest available scale.

The changes in the energy fluxes (and in the coupling between 2D and 3D modes) result in two different scaling laws, with one case displaying a spectrum $E(k_\perp) \sim k_\perp^{-3}$, and the other with a spectrum compatible with $E(k_\perp) \sim k_\perp^{-5/3}$. These two spectra can be explained using phenomenological arguments similar to those used by Kraichnan [41]. In the latter case, in which energy is injected directly into the 2D modes, and in which little energy goes into the 2D modes from the 3D modes, we can assume that the inverse cascade in the slow 2D modes is dominated by the turnover time $\tau_\perp \sim l_\perp/u_\perp$ (where l_\perp is a characteristic perpendicular length, and u_\perp is the 2D r.m.s. velocity at that length scale). With only one relevant timescale, Kraichnan phenomenology for the inverse cascade tells us that the energy flux in the 2D modes goes as

$$\Pi_{2D} \sim \frac{u_\perp^2}{\tau_\perp} \sim \frac{u_\perp^3}{l_\perp}, \quad (38)$$

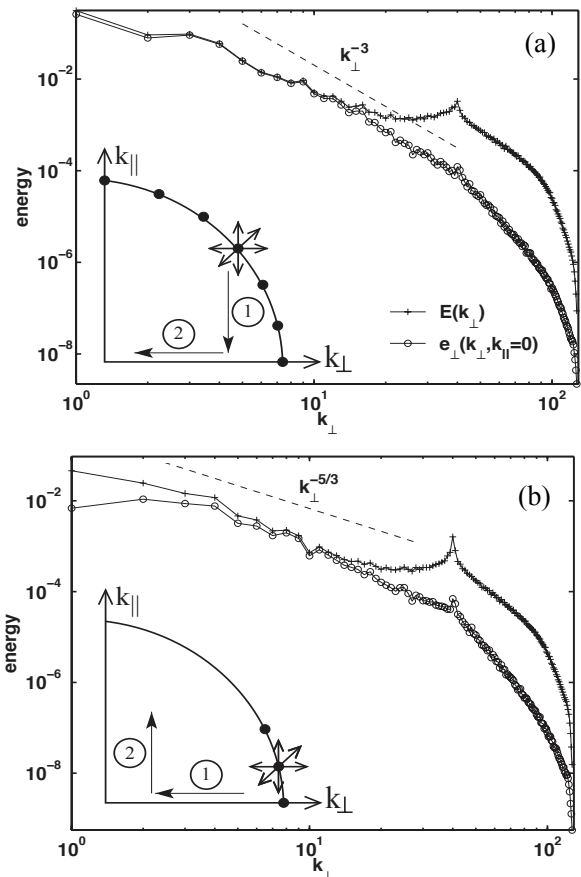


FIG. 2: (a) Reduced perpendicular energy spectrum $E(k_\perp)$ and perpendicular kinetic energy in the 2D modes $e_\perp(k_\perp, k_\parallel = 0)$ in a simulation of rotating turbulence forced at small scales with random isotropic forcing. The inset illustrates how the forcing acts over the spherical shell in Fourier space; energy is transferred first towards the 2D modes and then develops an inverse cascade. (b) Same for a simulation with anisotropic forcing. The inset illustrates how the energy that is injected directly into the 2D modes has an inverse cascade, and then it is transferred towards 3D modes as accumulation of energy at large scales saturates. In both figures power laws are shown as a reference (see [41] for more details).

which results in the $\sim k_\perp^{-5/3}$ energy spectrum.

On the other hand, if the forcing is isotropic and energy goes from the 3D modes to the 2D modes, interactions with the 3D modes cannot be neglected. Besides the slow turnover time τ_\perp , we now have to consider the time scale of the waves (which is the fastest time scale for many of the 3D modes), and which we can estimate as $\tau_\Omega \sim 1/\Omega$. Using Kraichnan phenomenology for interactions of waves and eddies [82], we can assume that the nonlinear transfer will be slowed down by a factor proportional to the Rossby number, i.e., to the ratio of time scales between the wave period and the non-linear

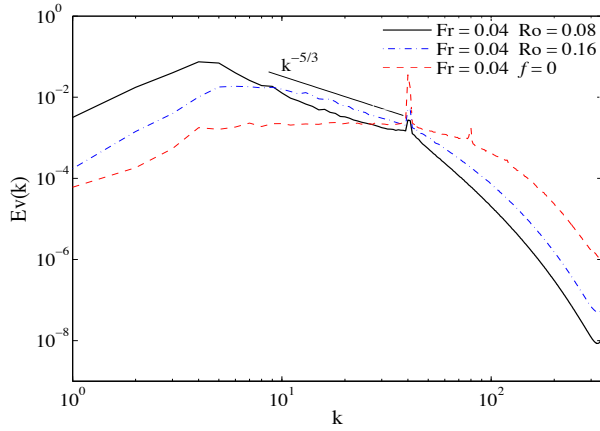


FIG. 3: (*Color online*) Isotropic kinetic energy spectrum in a 1024^3 simulation of a stably stratified flow ($f = 0$, i.e., without rotation), and in two 1024^3 simulations of rotating and stratified flows with the same Froude number and different Rossby numbers (modified from [58]). Note the growth of energy at wave numbers smaller than the forcing wavenumber $k_F \approx 40$ in the two latter simulations, and the flat spectrum at the same wave numbers in the former case. A $\sim k^{-5/3}$ power law is indicated as a reference.

turnover time. Then,

$$\Pi_{2D} \sim \left(\frac{u_{\perp}^2}{\tau_{nl}} \right) \left(\frac{\tau_{\Omega}}{\tau_{nl}} \right) \sim \frac{u_{\perp}^2}{\Omega \tau_{nl}^2}. \quad (39)$$

If the turnover time in the above expression is built upon the velocity at the forcing scale U (assuming most of the energy in the 2D modes comes directly from the 3D forced modes), this relation results in a $\sim k_{\perp}^{-3}$ scaling for the energy spectrum of the 2D modes [41].

B. Stratified case

A detailed study of the effect of the forcing on the development and growth of large scales in stratified flows (as well as in rotating and stratified flows) is still partially missing. For the sake of simplicity, from here on we will consider either isotropic forcing functions, or Taylor-Green forcing which does not inject energy directly into 2D modes, and which for the rotating case was shown to give an inverse cascade with the same scaling as isotropic forcing [41].

Figure 3 shows the isotropic energy spectrum in a 1024^3 simulation of a purely stratified flow with $\text{Re} \approx 1000$ and $\text{Fr} = 0.04$ ($f = 0$ as there is no rotation, see [58, 60] for more details). The flow is forced at $k_F \approx 40$ so there is room at small wave numbers for an inverse cascade to develop. Instead, what we observe is that energy grows at wave numbers $k < k_F$, but with a flat spectrum in this range.

In the purely stratified case there is growth of energy at large scales as energy piles up into VSHW, i.e., modes for

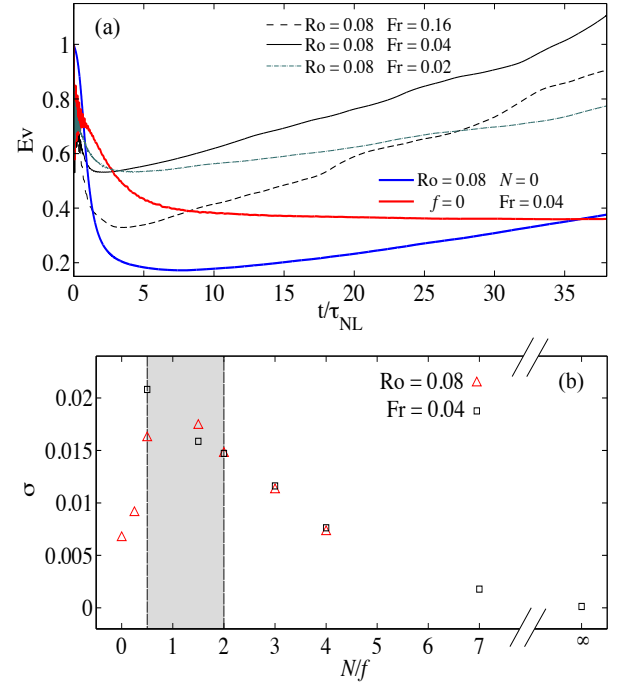


FIG. 4: (*Color online*) (a) Kinetic energy as a function of time in several 1024^3 simulations of rotating and stratified turbulence. The thick lines correspond to purely rotating or purely stratified simulations. The thin lines correspond to rotating and stratified runs. The two runs in the range $1/2 \leq N/f \leq 2$ have the fastest growth rate of $E_V(t)$. (b) Growth rate σ of the kinetic energy as a function of time, as a function of N/f for two sets of simulations: one with fixed $\text{Ro} = 0.08$ and varying Fr , and another with fixed $\text{Fr} = 0.04$ and varying Ro . The range $1/2 \leq N/f \leq 2$, which displays the largest growth rates, is indicated by the gray shading (data from [60], see this reference for more details).

the horizontal velocity with $k_{\perp} \approx 0$ and with strong vertical gradients [37]. However, this growth is not accompanied by a negative constant energy flux in a wide range of scales as expected for an inverse cascade [39, 40, 58]. Instead, the isotropic energy flux tends to be small at large scales (small wave numbers), while the parallel energy flux becomes negative and the perpendicular energy flux becomes positive [58]. In other words, the growth of energy at large scales is not the result of a self-similar cascade but rather of a very strong anisotropization of the flow. Candidates for the generation of the VSHW include resonant triads [37], and absorption of waves by critical layers [46].

C. Rotating and stratified case

As explained in the introduction and in Sec. II, the parameter N/f is expected to play an important role controlling the different regimes of the inverse cascade in rotating and stratified flows. At this point, we know that

while in the purely rotating case ($N/f \rightarrow 0$) there is an inverse cascade, in the purely stratified case ($N/f \rightarrow \infty$) there is none. Although *a priori* a monotonous decrease of the strength of the inverse cascade could be expected between these two limit cases, the non-monotonicity in the strength of the resonant interactions with N/f suggests there can be a distinct behavior in the range $1/2 \leq N/f \leq 2$.

This problem was considered in detail in [60], where a parametric study of the inverse cascade was done varying N/f in a large set of numerical simulations with spatial resolutions with up to 1024^3 grid points and Reynolds numbers up to ≈ 1000 . Figure 3 shows the isotropic kinetic energy spectrum for two 1024^3 runs of rotating and stratified flows forced at small scales with fixed Froude number ($Fr = 0.04$) and two different Rossby numbers ($Ro = 0.08$ and 0.16). Unlike the purely stratified case, both simulations display growth of energy at large scales, negative energy flux (not shown here), and a spectrum compatible with a $\sim k^{-5/3}$ power law at small scales. The simulations with $Ro = 0.08$ shows a larger peak of the energy spectrum, taking place at smaller wave numbers ($k \approx 4$). As both spectra are displayed at the same time, this indicates that the inverse cascade is faster in this simulation (which has $N/f = 2$), compared with the simulation with $Ro = 0.08$ which has $N/f = 4$.

The results of the detailed parametric study of the effect of varying N/f on the inverse cascade is summarized in Fig. 4. Figure 4(a) shows the kinetic energy as a function of time, $E_V(t)$, for several simulations with varying Ro and Fr numbers. The simulations are forced at small scales and started from random initial conditions at wave numbers $k > k_F$ (where k_F is the forcing wavenumber). First the energy decays as the system develops a turbulent spectrum, and after ≈ 5 turnover times two regimes can be observed. In the simulation without rotation ($f = 0$), $E_V(t)$ remains approximately constant. In the simulation without stratification ($N = 0$), energy grows monotonously in time. The same happens in the rotating and stratified cases, but the two simulations with $N/f = 1/2$ and $N/f = 2$ display the fastest growth of the energy.

A parametric study of this growth rate as a function of N/f for multiple runs is shown in Fig. 4(b). Two sets of simulations are shown, one with fixed Ro and varying N/f by varying the Fr number, and another with fixed Fr and varying Ro . In all cases, simulations with $1/2 \leq N/f \leq 2$ display the fastest growth of the energy. In [60] it was shown that this growth corresponds to a growth of the energy in 2D modes at large scales, and that it is caused by an inverse energy cascade with constant (and negative) energy flux which also takes maximum values in the range $1/2 \leq N/f \leq 2$. In [60] it was thus speculated that the larger efficiency of the inverse cascade in this range was associated with the absence of resonant interactions and the prevalence of QG behavior in this region of parameter space. In the rest of this paper we will consider new simulations and analysis to

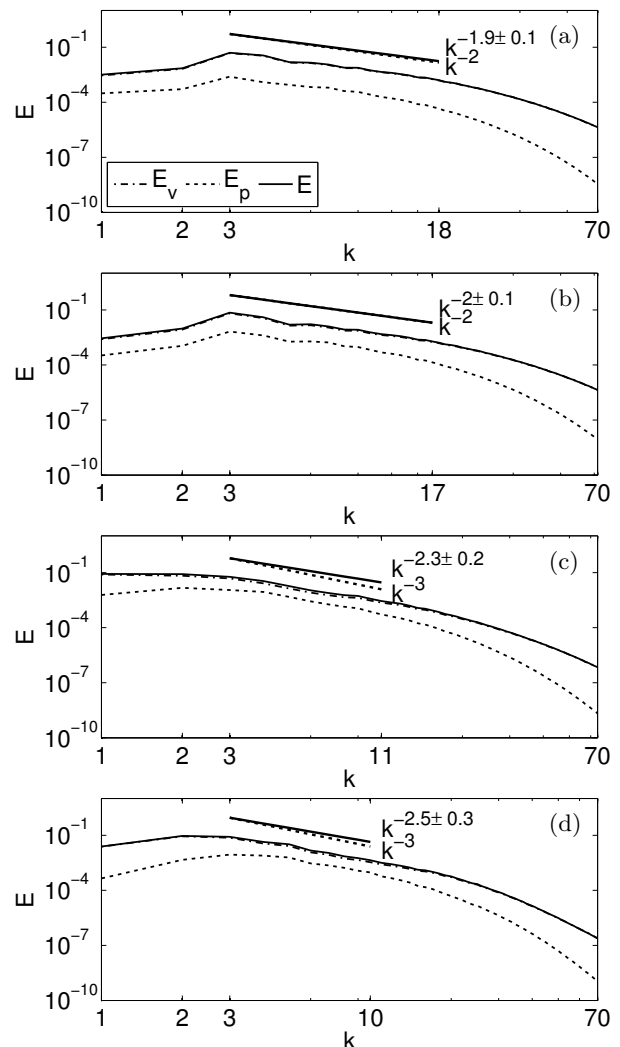


FIG. 5: Detail of the direct cascade inertial range in the isotropic spectra of kinetic energy E_V , potential energy E_P , and total energy E , in several 512^3 simulations of rotating and stratified turbulence, all forced at $k_F \approx 3$ and with $Ro \approx 0.2$. (a) $Fr = 0.8$, $N/f = 1/4$, (b) $Fr = 0.4$, $N/f = 1/2$, (c) $Fr = 0.1$, $N/f = 2$, and (d) $Fr = 0.05$, $N/f = 5$. Several power laws are shown as references.

confirm this is indeed the case.

IV. QUASI-GEOSTROPHIC BEHAVIOR

For the analysis in this section and in the next, we performed a new set of simulations of rotating and stratified turbulence. As in Sec. V we will perform a spatio-temporal analysis of the data to extract the strength of the waves (which requires storage of the data with very high cadence in time), we will only be able to consider moderate spatial resolutions. Therefore, while simulations in the previous sections had spatial resolutions of 1024^3 grid points or larger, simulations in the next two

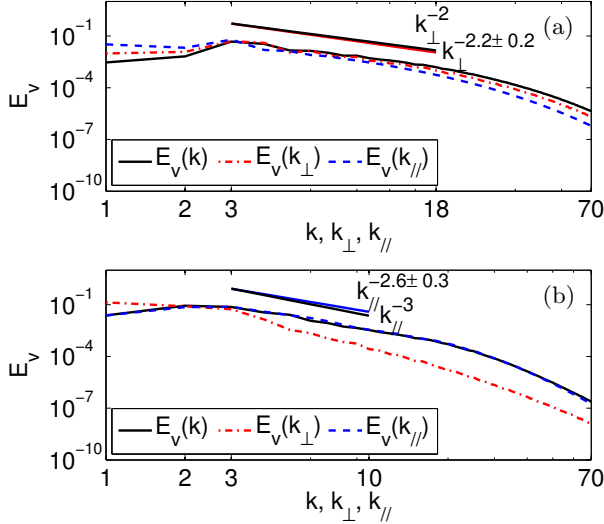


FIG. 6: (Color online) Detail of the direct cascade inertial range in the isotropic spectrum of kinetic energy $E_V(k)$, reduced perpendicular spectrum of kinetic energy $E_V(k_\perp)$, and reduced parallel spectrum of kinetic energy $E_V(k_\parallel)$, for two 512^3 simulations of rotating and stratified turbulence forced at $k_F \approx 3$ with $Ro \approx 0.2$. (a) $Fr = 0.8$, $N/f = 1/4$, and (b) $Fr = 0.05$, $N/f = 5$. Several power laws are shown as references.

sections will consist of two large datasets of runs with 256^3 and 512^3 grid points. As in the previous sections, we will explore parameter space by considering multiple values of Fr , and for each of these values we will vary Ro to explore the effect of changing N/f . Overall, we performed 15 simulations with 256^3 grid points with $Re \approx 1000$, $0.02 \lesssim Fr \lesssim 1.8$, $0.04 \lesssim Ro \lesssim 0.3$, and $0.1 \lesssim N/f \lesssim 10$, and 8 simulations with 512^3 grid points with $Re \approx 2000$, $0.05 \lesssim Fr \lesssim 0.8$, $0.04 \lesssim Ro \lesssim 0.02$, and $0.25 \lesssim N/f \lesssim 5$.

Also, as resolution in these simulations is limited, we forced the flow at much larger scales leaving very little room for the growth of energy at large scales. We thus use Taylor-Green forcing [90] acting at $k_F = 3\sqrt{2} \approx 3$. Large scale forcing is required as one of our goals will be to identify the role of the waves at small scales, but it will force us to complement the results in these sections with the results in the previous sections where time resolution was not as good, but the inverse cascade ranges were better resolved. To study both ranges separately is a common practice in geophysical fluid dynamics due to constraints in computing power, as only very recently simulations were able to resolve dual cascades in a unique simulation at very high resolution [91].

Figure 5 shows a detail, in the vicinity of the inertial range, of the isotropic energy spectrum $E(k)$ for four 512^3 runs with $Ro \approx 0.2$ and varying Fr (and therefore, varying N/f). Power laws $\sim k^{-2}$ and $\sim k^{-3}$ are shown as references. Also as a reference we present a best fit to a power law in the range of scales $k \in [k_F, k_{1/2}]$, where $k_{1/2}$

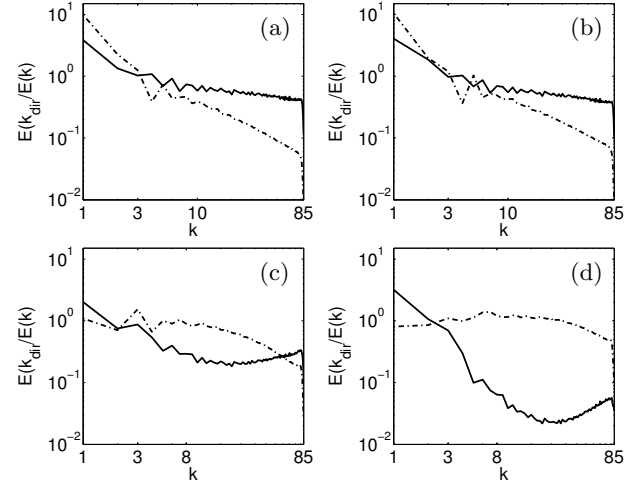


FIG. 7: Ratio of the spectra $E(k_\perp)/E(k)$ (solid) and $E(k_\parallel)/E(k)$ (dash-dotted) for several 256^3 simulations of rotating and stratified turbulence forced at $k_F \approx 3$ with $Ro \approx 0.2$. (a) $Fr = 0.8$, $N/f = 1/4$, (b) $Fr = 0.4$, $N/f = 1/2$, (c) $Fr = 0.1$, $N/f = 2$, and (d) $Fr = 0.05$, $N/f = 5$.

is the wave number at which the energy flux drops to $1/2$ of its value at the injection scale, i.e., $\Pi(k_{1/2}) = \Pi(k_F)/2$. This fit is not intended to claim a specific power law followed by the inertial range, as the value of $1/2$ used to define the drop in the flux is arbitrary, but rather to illustrate that as N/f increases, the energy spectrum becomes steeper, going from the behavior expected for a purely rotating flow ($\sim k^{-2}$) to that of a purely stratified flow ($\sim k^{-3}$). Also, a small growth of energy at wave numbers $k < k_F$ can be observed in some of these runs. Although the scale separation at large scales (small wave numbers) in these runs is small to study the inverse cascade, inverse transfer can be observed, as will be also shown in the energy fluxes.

Figure 6 shows the isotropic and reduced parallel and perpendicular spectra of the kinetic energy for two of the simulations shown in Fig. 5. Again, power laws and best fits to the spectrum are shown as references. While in the inertial range for the case with $N/f = 1/4$ the reduced perpendicular spectrum $E(k_\perp)$ is closer to the isotropic spectrum $E(k)$, in the case with $N/f = 5$ the reduced parallel spectrum $E(k_\parallel)$ is closer to $E(k)$. In other words, in the case with stronger rotation most of the energy seems to accumulate near modes with $k_\parallel \approx 0$, while in the case with stronger stratification energy accumulates near modes with $k_\perp \approx 0$.

This is further illustrated in Fig. 7, which shows the ratios $E(k_\perp)/E(k)$ and $E(k_\parallel)/E(k)$ for several simulations with varying N/f . For $N/f < 1$ and for $k > k_F$, the ratio $E(k_\perp)/E(k)$ is of order one in a wide range of wave numbers, while $E(k_\parallel)/E(k)$ decreases rapidly with increasing wave number. On the other hand, for $N/f > 1$ the ratio $E(k_\parallel)/E(k)$ remains of order one in a range of wave numbers with $k > k_F$, while $E(k_\perp)/E(k)$ decreases rapidly. It is clear from these figures that these simula-

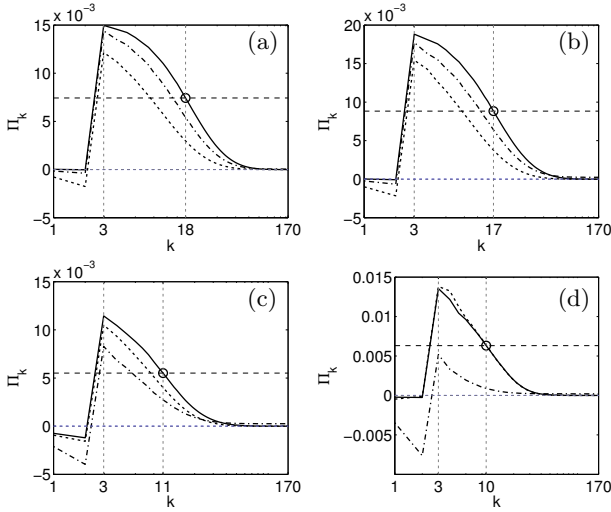


FIG. 8: Isotropic energy flux $\Pi(k)$ (solid), perpendicular energy flux $\Pi(k_\perp)$ (dashed), and parallel energy flux $\Pi(k_\parallel)$ (dash-dotted) in several 512^3 simulations of rotating and stratified turbulence forced at $k_F = 3$ with $Ro \approx 0.2$. From left to right and top to bottom: (a) $Fr = 0.8$, $N/f = 1/4$, (b) $Fr = 0.4$, $N/f = 1/2$, (c) $Fr = 0.1$, $N/f = 2$, and (d) $Fr = 0.05$, $N/f = 5$. The straight lines and the circles indicate the wave number at which the flux drops to $1/2$ of its value at the forcing wave number $k_F \approx 3$. Note that the largest negative isotropic and perpendicular fluxes (for $k < k_F$) are obtained in the case with $N/f = 2$. The simulation with $N/f = 5$ has negative parallel flux, but negligible isotropic and perpendicular inverse fluxes at large scales.

tions do not recover isotropy at small scales, i.e., that the Ozmidov and Zeman scales are not resolved [51, 67–69].

Figure 8 shows the energy fluxes (isotropic, parallel, and perpendicular) in the same four simulations as in Fig. 5. Note that besides the positive flux for $k > k_F$, there is a small backtransfer with negative flux towards large scales for $k < k_F$. Just as in the results shown in the previous section, with larger scale separation and a clear inverse cascade, here the amplitude of the net negative flux is not monotonic with N/f , and it becomes larger in the run with $N/f = 2$. As a comparison, the run with $N/f = 1/4$ shows a smaller inverse flux, and the run with $N/f = 5$ shows a larger inverse parallel flux but negligible isotropic and perpendicular inverse fluxes. In the latter case, and when larger scale separations are considered, this is just the result of a very anisotropic flux at large scales that results in the formation of VSHW [58].

We can now use these simulations to study the role of triadic interactions in the cascade, as well as the role of waves and slow modes as we vary N/f . We start by considering anisotropy and the scaling of typical length scales, as done before by other authors [20, 39, 40, 92], to then present spatio-temporal analyses in the next section. We must then define first parallel and perpendicular characteristic length scales, which can be easily done

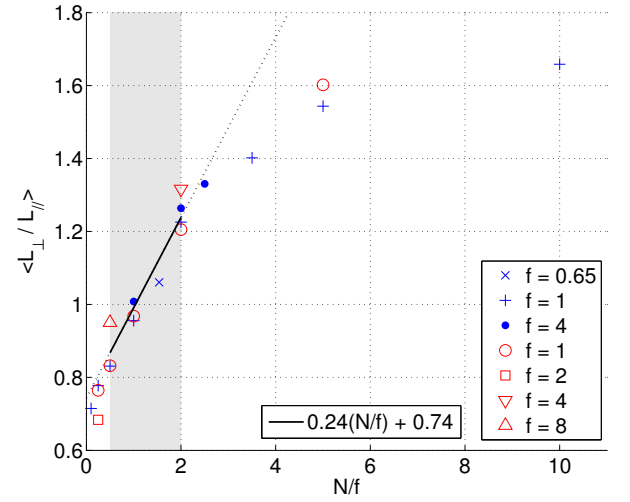


FIG. 9: (Color online) Ratio of the perpendicular to parallel integral scales $\langle L_\perp/L_\parallel \rangle$ (averaged over time in the turbulent steady state) as a function of N/f for several 256^3 and 512^3 simulations of rotating and stratified turbulence with varying Ro and Fr numbers. The range with no resonant interactions, $1/2 \leq N/f \leq 2$, is indicated by the gray shading. In this range, a linear fit of $\langle L_\perp/L_\parallel \rangle$ as a function of N/f (expected from quasi-geostrophy) is shown as a reference.

from the reduced energy spectra:

$$L_\perp = 2\pi \frac{\sum_{k_\perp=1}^{k_{max}} E(k_\perp)/k_\perp}{\sum_{k_\perp=1}^{k_{max}} E(k_\perp)}, \quad (40)$$

$$L_\parallel = 2\pi \frac{\sum_{k_\parallel=1}^{k_{max}} E(k_\parallel)/k_\parallel}{\sum_{k_\parallel=1}^{k_{max}} E(k_\parallel)}, \quad (41)$$

where these scales correspond just to an extension of the usual isotropic integral scale to the anisotropic case. Here, k_{max} is the maximum resolved wavenumber in the simulation, which for pseudospectral simulations using the $2/3$ -rule for dealiasing correspond to $k_{max} = N_l/3$ with N_l the linear grid resolution.

Figure 9 shows the ratio of these two scales (averaged in time) as a function of N/f for several runs. In agreement with what we observed in the anisotropic spectra (Fig. 7), the ratio $\langle L_\perp/L_\parallel \rangle$ goes from values smaller than one for $N/f < 1$, reaches $\langle L_\perp/L_\parallel \rangle \approx 1$ for $N/f \approx 1$, and becomes larger than one for $N/f > 1$, apparently saturating for large values of N/f . Moreover, this behavior is independent of the value of f (i.e., of the Froude number) as all runs seem to collapse to the same curve. But note also that there is a range of N/f for which $\langle L_\perp/L_\parallel \rangle$ seems to scale linearly with N/f , and which seems to be in agreement with the region indicated in all previous figures corresponding to the range in which there are no resonant interactions, $1/2 \leq N/f \leq 2$. In this region QG modes are expected to dominate, whereby the linear relationship can be expected from Charney's argument [20] that a turbulent QG flow is isotropic in the re-scaled

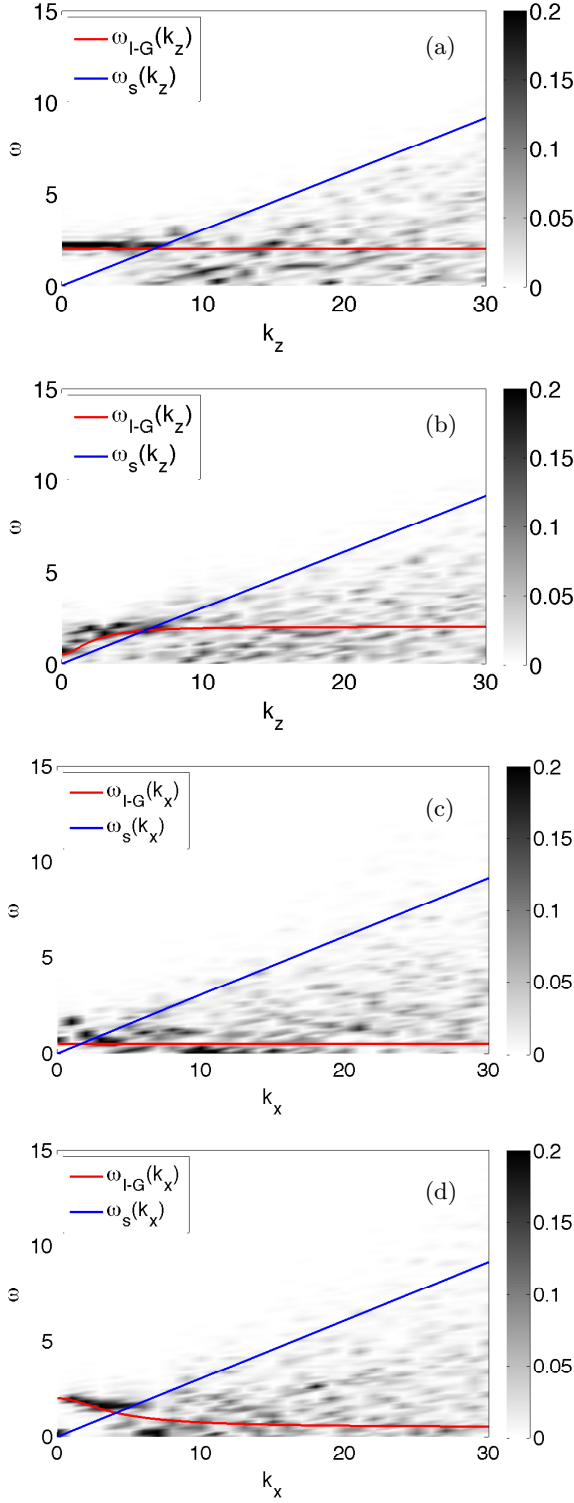


FIG. 10: (*Color online*) Spatio-temporal power spectra $|u_x|^2(k_x, k_y, k_z, \omega)$ and $|u_z|^2(k_x, k_y, k_z, \omega)$ for a 512^3 simulation of rotating and stratified turbulence with $Fr = 0.3$, $Ro = 0.075$ ($N/f = 1/4$). Two-dimensional slices of each four-dimensional spectrum are shown by fixing two components of the wave vector. (a) $|u_x|^2(k_x = 0, k_y = 0, k_z, \omega)$, (b) $|u_x|^2(k_x = 3, k_y = 0, k_z, \omega)$, (c) $|u_z|^2(k_x, k_y = 0, k_z = 0, \omega)$, and (d) $|u_z|^2(k_x, k_y = 0, k_z = 3, \omega)$. The solid lines indicate the dispersion relation of inertia-gravity waves, $\omega_{I-G}(\mathbf{k})$, and of sweeping, $\omega_s(\mathbf{k})$.

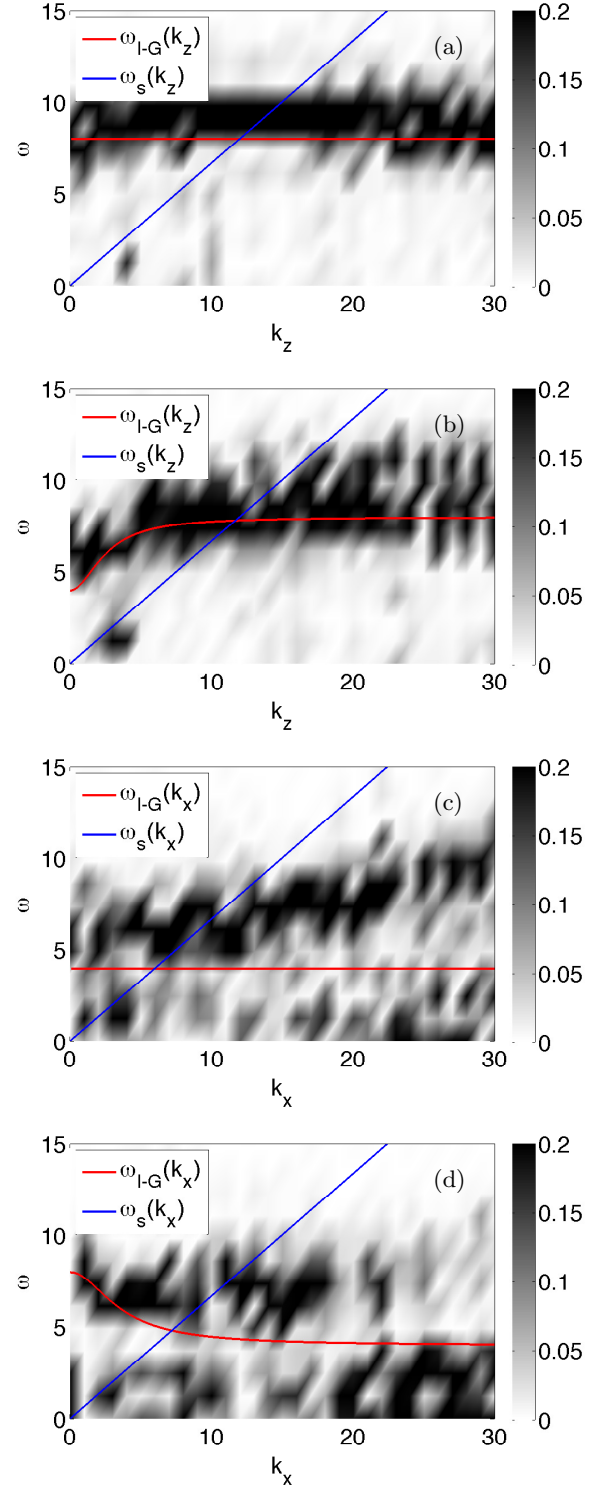


FIG. 11: (*Color online*) Spatio-temporal power spectra $|u_x|^2(k_x, k_y, k_z, \omega)$ and $|u_z|^2(k_x, k_y, k_z, \omega)$ for a 512^3 simulation of rotating and stratified turbulence with $Fr = 0.08$, $Ro = 0.04$ ($N/f = 1/2$). Two-dimensional slices of each four-dimensional spectrum are shown by fixing two components of the wave vector. (a) $|u_x|^2(k_x = 0, k_y = 0, k_z, \omega)$, (b) $|u_x|^2(k_x = 3, k_y = 0, k_z, \omega)$, (c) $|u_z|^2(k_x, k_y = 0, k_z = 0, \omega)$, and (d) $|u_z|^2(k_x, k_y = 0, k_z = 3, \omega)$. The solid lines indicate the dispersion relation of inertia-gravity waves, $\omega_{I-G}(\mathbf{k})$, and of sweeping, $\omega_s(\mathbf{k})$.

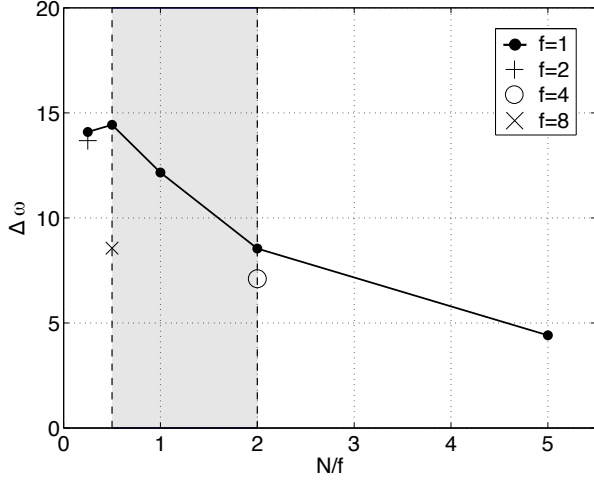


FIG. 12: Measured dispersion of the energy around the theoretical dispersion relation of inertia-gravity waves, as a function of N/f for several 256^3 and 512^3 simulations of rotating and stratified turbulence with varying Ro and Fr numbers. The range with no resonant interactions, $1/2 \leq N/f \leq 2$, is indicated by the gray area. The dispersion for $f = 1$ takes its maximum in this region. A few points for other values of f are also shown.

coordinate $(N/f)z$, which implies a linear relation for the vertical integral scale $L_{\parallel} \sim (f/N)L_{\perp}$, or equivalently

$$\left\langle \frac{L_{\perp}}{L_{\parallel}} \right\rangle = A \frac{N}{f} + B. \quad (42)$$

In Fig. 9 we also show a best fit for this relation to our data. This scaling was reported before in numerical simulations of QG turbulence [92], where the authors found $\langle L_{\perp}/L_{\parallel} \rangle \approx 1.3(N/f)$. As our definitions of the vertical and parallel length scales are not equivalent to those used in [92], the prefactor cannot be directly compared. But in both cases it is remarkable that a linear relation holds, specially in the $1/2 \leq N/f \leq 2$ range in our case.

V. SPATIO-TEMPORAL SPECTRUM

In this section we present the spatio-temporal spectrum of several of the simulations discussed in Sec. IV. While extraction of waves and slow modes is often done using normal mode decompositions of the frozen in time fields in Fourier space [54, 93, 94], precise detection of waves, mean winds, and eddies require information resolved in space and in time. In [95] we introduced the spatio-temporal spectrum as a way to do this decomposition, and showed multiple applications including purely rotating [83] and purely stratified flows [46]. The main objective of this section is to consider the rotating and stratified case, in particular in the range $1/2 \leq N/f \leq 2$, and to use the spatio-temporal spectrum to quantify the relevance of wave modes and of slow modes. As discussed in Secs. III and IV, several effects in this range

are believed to be associated with a dominance of slow modes and a relatively less importance of wave modes. The spatio-temporal spectrum will allow us to explicitly verify this is the case. However, as computation of the spatio-temporal spectrum requires very high temporal cadence, we will be able to do this analysis only in the simulations with 512^3 grid points.

Detection of the waves in the spatio-temporal spectrum requires some knowledge of what components of the fields are affected by the waves, depending on their polarization. For systems with $N/f \ll 1$, rotation is dominant and inertia-gravity waves reduce to inertial waves. Thus, in this case we should look at the spectrum of u_x as for inertial waves the perturbation takes place in the plane perpendicular to Ω . In contrast, for strongly stratified systems with $N/f \gg 1$ we should consider u_z as this is the component of the velocity that is coupled to the temperature fluctuations in internal gravity waves. Thus, we consider the power spectrum of both components to allow identification of the waves as N/f is varied.

The spatio-temporal spectrum was computed for all 512^3 simulations. Figures 10 and 11 show an illustration of these spectra for the runs with $N/f = 1/4$ and with $N/f = 1/2$ (the first run in the range $1/2 \leq N/f \leq 2$). As the spectrum is four-dimensional (it depends on the wave vector \mathbf{k} and the frequency ω), for u_x we show slices for fixed values of k_x and k_y , and show the spectrum as a function of k_z and ω , while for u_z we show slices for fixed values of k_y and k_z , and show the spectrum as a function of k_x and ω . The figures also indicate as a reference the theoretical dispersion relation of inertia-gravity waves, and the sweeping relation.

As a rule, excitation of modes lying over the theoretical dispersion relation can be observed for wave numbers such that the frequency of the waves is larger than the frequency of sweeping (i.e., for modes for which the waves are faster than the sweeping). This is to be expected as in wave turbulence, the fastest time scale controls the decorrelation of the modes [83]. But more interestingly, the dispersion of the energy around the dispersion relation of the waves varies with N/f . While the simulation with $N/f = 1/4$ shows (for small wave numbers) a strong concentration of energy around the relation $\omega_{I-G}(\mathbf{k})$ (i.e., the theoretical dispersion relation of inertia-gravity waves), for $N/f = 1/2$ the dispersion of the energy around this dispersion relation is much larger, and in some of the figures energy is concentrated in modes that do not correspond to wave excitations.

A detailed analysis of the spatio-temporal spectra for all simulations is summarized in Figs. 12 and 13. Figure 12 shows the dispersion of the energy around the theoretical wave dispersion relation as a function of N/f for all 512^3 runs. The dispersion, e.g., for the power spectrum of the x component of the velocity, is defined as

$$\Delta\omega = \frac{\sum_{\mathbf{k}, \omega} |\omega(\mathbf{k}) - \omega_{I-G}(\mathbf{k})|^2 |u_x(\mathbf{k}, \omega)|^2}{\sum_{\mathbf{k}, \omega} |u_x(\mathbf{k}, \omega)|^2}, \quad (43)$$

and it corresponds to the the mean square differences

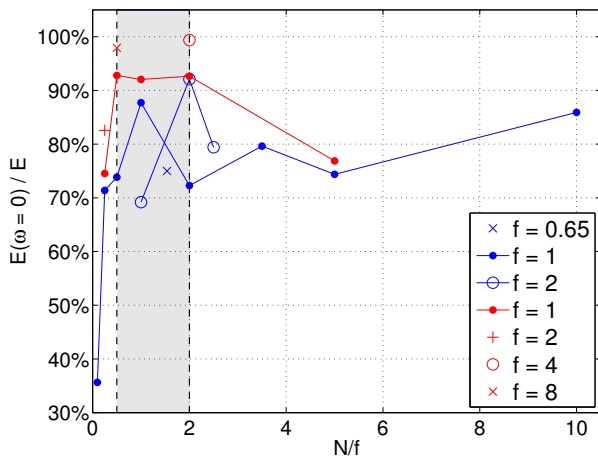


FIG. 13: (*Color online*) Ratio of energy in modes with zero frequency to the total energy as a function of N/f for several 256^3 and 512^3 simulations of rotating and stratified turbulence with varying Ro and Fr numbers. The range with no resonant interactions, $1/2 \leq N/f \leq 2$, is indicated by the gray area. Note that the ratio takes the largest values in this region.

between $\omega_{L-G}(\mathbf{k})$ and the actual data, weighted by the spectral amplitude squared. As expected from the theoretical arguments, the maximum dispersion takes place in the range $1/2 \leq N/f \leq 2$, also confirming the arguments in the previous sections. A few points for simulations with different values of f are shown, which (for fixed N/f) show a smaller dispersion as f is increased, to be expected as dispersion should decrease (i.e., more energy should be in the wave modes) as the strength of rotation and stratification increases.

From this data we can also compute the amount of energy in slow modes, that is to say, in modes with zero frequency. This is shown in Fig. 13, normalized by the total energy, for all simulations. In the figure there is a growth in this ratio in the region of non-resonant triads. Increasing the value of f (and thus decreasing the Froude number) seems to increase the ratio, thus augmenting the amount of energy in modes with zero frequency. These results are consistent with those reported in [40], where Waite and Bartello observed, for $Ro \approx 10^{-1}$, a growth in vortical energy as Ro decreases with fixed N . With three different values of N (4, 8 and 16), they also concluded that the ratio of vortical energy to total energy is independent of the Rossby number. Our data, however, shows a dependence on the value of Ro , with smaller Ro resulting in more energy in the slow modes.

VI. CONCLUSIONS

Inverse cascades play a central role in geophysical turbulence, providing a mechanism for the formation of large-scale structures and for the self-organization of dis-

organized flows. Since Kraichnan contribution, extensions of his ideas to quasi-geostrophic turbulence, rotating flows, and rotating and stratified flows have been developed as a way to better describe atmospheric and oceanic processes. In this context, here we reviewed several recent studies of inverse cascades in rotating and stratified turbulence.

Special emphasis was put on reviewing the dependence of scaling laws, anisotropy, and the strength of the inverse cascade on the ratio N/f of the Brunt-Väisälä frequency to the Coriolis frequency. We showed that while the anisotropy and the ratio of perpendicular to parallel length scales varies linearly with N/f (in particular in the range $1/2 \leq N/f \leq 2$), the strength of the inverse cascade depends non-monotonically on this parameter, with the inverse cascade being faster in this range, and then decreasing monotonically as N/f is increased.

This behavior can be explained by considering that in the range $1/2 \leq N/f \leq 2$ no resonant triadic interactions between waves are available. Thus, quasi-geostrophic motions are expected to dominate the dynamics. Previous studies (see, e.g., [39, 40, 53–55, 92]) have confirmed this by indirect measures, such as, e.g., normal mode decomposition of frozen in time fields, to separate wave modes from slow modes. Here we presented a new analysis based on fully resolved spatio-temporal information, using the spectrum as a function of the wave vector and frequency to measure how much energy is excited in modes compatible with the dispersion relation of the waves, and in the rest of the modes.

The simulations confirmed the linear scaling of the ratio of the perpendicular to parallel velocity with N/f in the range $1/2 \leq N/f \leq 2$, and also showed that accumulation of energy near wave modes in the spatio-temporal spectrum is minimal in this range, while energy in slow modes becomes larger. This is in good agreement with previous results using different methods for the analysis, and sheds new light on reasons for the fast inverse cascade of 3D rotating and stratified turbulent flows reported previously in [60].

Fifty years after the paper by Kraichnan on inverse cascades in two dimensional flows [1], there remains much to be done to understand turbulent phenomena in the real world. The study of inverse cascades in more realistic scenarios has just started, and the previous works reviewed here, as well as the new results, consider small Reynolds numbers, periodic boundary conditions, or infinite domains which put them far away from real applications. As in the paper written by Kraichnan and Montgomery [2], it is however our hope that some of the results of these studies can be translated to atmospheric and oceanographic problems. Recent studies considering observations in the atmosphere and the ocean (see, e.g., [29–31] and references therein) seem to indicate that indeed the gap between idealized simulations and real measurements of the inverse cascade can be bridged.

Acknowledgments

D.O. and P.D.M. acknowledge support from UBA-CYT Grant No. 20020130100738BA, and PICT Grants Nos. 2011-1529 and 2015-3530. P.D.M. also acknowledges support from the CISL visitor program at NCAR.

RM acknowledges support from the PRESTIGE program coordinated by Campus France (co-financed under Marie Curie FP7 PCOFUND-GA-2013-609102), and the PALSE program at the University of Lyon, through the PALSE postdoctoral fellowship and the IMPULSION action.

-
- [1] R. Kraichnan, Phys. Fluids **10**, 1417 (1967).
 - [2] R. Kraichnan and D. Montgomery, Rep. Prog. Phys. **43**, 547 (1980).
 - [3] H. J. H. Clercx and G. J. F. van Heijst, Phys. Rev. Lett. **85**, 306 (2000).
 - [4] A. Bracco, J. C. McWilliams, G. Murante, A. Provenzale, and J. B. Weiss, Phys. Fluids **12**, 2931 (2000).
 - [5] H. Kellay and W. I. Goldburg, Rep. Prog. Phys. **64**, 845 (2002).
 - [6] L. Biferale, S. Musacchio, and F. Toschi, Phys. Rev. Lett. **108**, 164501 (2012).
 - [7] G. Boffetta and R. E. Ecke, Ann. Rev. Fluid Mech. **44**, 427 (2011).
 - [8] P. D. Mininni and A. Pouquet, Phys. Rev. E **87**, 033002 (2013).
 - [9] A. Pouquet, J. Fluid Mech. **88**, 1 (1978).
 - [10] A. C. Ting, W. H. Matthaeus, and D. Montgomery, Phys. Fluids **29**, 3261 (1986).
 - [11] M. Christensson, M. Hindmarsh, and A. Brandenburg, Phys. Rev. E **64**, 056405 (2001).
 - [12] P. D. Mininni, D. C. Montgomery, and A. G. Pouquet, Phys. Fluids **17**, 035112 (2005).
 - [13] A. Alexakis, P. D. Mininni, and A. Pouquet, Astrophys. J. **640**, 335 (2006).
 - [14] P. D. Mininni, Phys. Rev. E **76**, 026316 (2007).
 - [15] P. Démoulin and E. Pariat, Adv. Sp. Res. **43**, 1013 (2009).
 - [16] E. N. Lorenz, Tellus **21**, 289 (1969).
 - [17] C. E. Leith, J. Atmos. Sc. **28**, 145 (1971).
 - [18] C. E. Leith and R. H. Kraichnan, J. Atmos. Sc. **29**, 1041 (1972).
 - [19] G. Boffetta and S. Musacchio, Phys. Fluids **13**, 1060 (2001).
 - [20] J. G. Charney, J. Atmos. Sc. **28**, 1087 (1971).
 - [21] J. R. Herring, Met. and Atmos. Phys. **38**, 106 (1988).
 - [22] G. Boffetta, F. De Lillo, and S. Musacchio, EPL (Europhys. Lett.) **59**, 687 (2002).
 - [23] S. Fox and P. A. Davidson, Phys. Fluids **21**, 125102 (2009).
 - [24] A. Vallgren and E. Lindborg, J. Fluid Mech. **656**, 448 (2010).
 - [25] W.-C. Müller and M. Thiele, EPL (Europhys. Lett.) **77**, 34003 (2007).
 - [26] P. A. Davidson, *Turbulence in rotating stratified and electrically conducting fluids* (Cambridge Univ. Press, Cambridge, 2013).
 - [27] G. D. Nastrom, K. S. Gage, and W. H. Jaspersion, Nature **310**, 36 (1984).
 - [28] G. D. Nastrom and K. S. Gage, J. Atmos. Sc. **42**, 950 (1985).
 - [29] S. Sukoriansky, N. Dikovskaya, and B. Galperin, J. Atmos. Sc. **64**, 3312 (2007).
 - [30] R. B. Scott and F. Wang, J. Phys. Ocean. **35**, 1650 (2005).
 - [31] F. Schlösser and C. Eden, Geophys. Res. Lett. **34**, L02604 (2007).
 - [32] M. Verma, EPL (Europhys. Lett.) **98**, 14003 (2011).
 - [33] D. K. Lilly, J. Atmos. Sc. **40**, 749 (1983).
 - [34] R. Salmon, *Lectures on geophysical fluid dynamics* (Oxford Univ. Press, New York, 1998).
 - [35] E. Lindborg, Geophys. Res. Lett. **32**, 1 (2005).
 - [36] J. Riley and E. Lindborg, J. Atmos. Sc. **65**, 2416 (2008).
 - [37] L. M. Smith and F. Waleffe, J. Fluid Mech. **451**, 145 (2002).
 - [38] J.-P. Laval, J. C. McWilliams, and B. Dubrulle, Phys. Rev. E **68**, 036308 (2003).
 - [39] M. L. Waite and P. Bartello, J. Fluid Mech. **517**, 281 (2004).
 - [40] M. L. Waite and P. Bartello, J. Fluid Mech. **568**, 89 (2006).
 - [41] A. Sen, P. D. Mininni, D. Rosenberg, and A. Pouquet, Phys. Rev. E **86**, 036319 (2012).
 - [42] C. Rorai, D. Rosenberg, A. Pouquet, and P. D. Mininni, Phys. Rev. E **87**, 063007 (2013).
 - [43] C. Rorai, P. D. Mininni, and A. Pouquet, Phys. Rev. E **89**, 043002 (2014).
 - [44] K. Polzin and Y. Lvov, Rev. Geophys. **49**, RG4003 (2011).
 - [45] G. Ivey, K. Winters, and J. Koseff, Ann. Rev. Fluid Mech. **40**, 169 (2008).
 - [46] C. di Leoni and P. D. Mininni, Phys. Rev. E **91**, 033015 (2015).
 - [47] G. Brethouwer, P. Billant, E. Lindborg, and J.-M. Chomaz, J. Fluid Mech. **585**, 343 (2007).
 - [48] E. Lindborg and G. Brethouwer, J. Fluid Mech. **586**, 83 (2007).
 - [49] H. Aluie and S. Kurien, EPL (Europhys. Lett.) **96**, 44006 (2011).
 - [50] M. L. Waite, Phys. Fluids **23**, 066602 (2011).
 - [51] S. Almalkie and S. de Bruyn Kops, J. Turbulence **13**, 29 (2012).
 - [52] Y. Kimura and J. R. Herring, J. Fluid Mech. **698**, 19 (2012).
 - [53] P. Bartello, J. Atmos. Sc. **52**, 4410 (1995).
 - [54] O. Métais, P. Bartello, E. Garnier, J. Riley, and M. Lesieur, Dyn. Oc. Atm. **23**, 193 (1996).
 - [55] S. Kurien, B. Wingate, and M. Taylor, EPL (Europhys. Lett.) **84**, 24003 (2008).
 - [56] L. Smith, J. Chasnov, and F. Waleffe, Phys. Rev. Lett. **77**, 2467 (1996).
 - [57] P. D. Mininni and A. Pouquet, Phys. Fluids **22**, 035105 (2010).
 - [58] R. Marino, P. D. Mininni, D. L. Rosenberg, and A. Pouquet, Phys. Rev. E **90**, 023018 (2014).
 - [59] H. Hanazaki, J. Fluid Mech. **465**, 157 (2002).
 - [60] R. Marino, P. D. Mininni, D. Rosenberg, and A. Pouquet,

- EPL (Europhys. Lett.) **102**, 44006 (2013).
- [61] C. Cambon and L. Jacquin, J. Fluid Mech. **202**, 295 (1989).
 - [62] F. Waleffe, Phys. Fluids **4**, 350 (1992).
 - [63] F. Waleffe, Phys. Fluids A **5**, 677 (1993).
 - [64] C. Cambon, N. N. Mansour, and F. S. Godeferd, J. Fluid Mech. **337**, 303 (1997).
 - [65] C. Cambon, Eur. J. Mech. B – Fluids **20**, 489 (2001).
 - [66] L. Shih, J. Koseff, G. Ivey, and J. Ferziger, J. Fluid Mech. **525**, 193 (2005).
 - [67] P. D. Mininni, D. Rosenberg, and A. Pouquet, J. Fluid Mech. **699**, 263 (2012).
 - [68] A. Delache, C. Cambon, and F. Godeferd, Phys. Fluids **26**, 025104 (2014).
 - [69] C. Rorai, P. D. Mininni, and A. Pouquet, Phys. Rev. E **92**, 013003 (2015).
 - [70] J. Y. N. Cho, Y. Zhu, Y. Newell, R. E. Anderson, J. D. Barrick, G. L. Gregory, G. W. Sachse, M. A. Carroll, and G. M. Albercook, J. Geophys. Res. **104**, 5697 (1999).
 - [71] D. G. Vincent and T. W. Schlatter, Tellus **31**, 493 (1979).
 - [72] L. Liechtenstein, F. S. Godeferd, and C. Cambon, J. Turbulence **6**, N24 (2005).
 - [73] P. Billant and J.-M. Chomaz, Phys. Fluids **13**, 1645 (2001).
 - [74] A. Babin, A. Mahalov, B. Nicolaenko, and Y. Zhou, Theo. and Comp. Fluid Dyn. **9**, 223 (1997).
 - [75] K. Julien, E. Knobloch, and J. Werne, Theo. and Comp. Fluid Dyn. **11**, 251 (1998).
 - [76] L. M. Smith and F. Waleffe, PoF **11**, 1608 (1999).
 - [77] F. Bellet, F. S. Godeferd, and F. S. Scott, J. Fluid Mech. **562**, 83 (2006).
 - [78] A. Kafiabad and P. Bartello, J. Fluid Mech. **795**, 914 (2016).
 - [79] A. Alexakis, J. Fluid Mech. **769**, 46 (2015).
 - [80] P. C. di Leoni and P. Mininni, J. Fluid Mech. **809**, 821 (2016).
 - [81] S. Nazarenko, *Wave Turbulence* (Springer, New York, 2011).
 - [82] R. H. Kraichnan, Phys. Fluids **8**, 1385 (1965).
 - [83] P. C. di Leoni, P. J. Cobelli, P. D. Mininni, P. Dmitruk, and W. H. Matthaeus, Phys. Fluids **26**, 035106 (2014).
 - [84] S. Chen and R. H. Kraichnan, Phys. Fluids A **1**, 2019 (1989).
 - [85] B. Dubrulle and L. Valdetaro, Astron. Astrophys. **263**, 387 (1992).
 - [86] Y. Zhou, Phys. Fluids **7**, 2092 (1995).
 - [87] A. Pouquet and P. Mininni, Phil. Trans. Roy. Soc. **368**, 1635 (2010).
 - [88] A. Campagne, B. Gallet, F. Moisy, and P.-P. Cortet, Phys. Fluids **26**, 125112 (2014).
 - [89] C. Cambon, R. Rubinstein, and F. S. Godeferd, New J. Phys. **6**, 73 (2004).
 - [90] P. Mininni, A. Alexakis, and A. Pouquet, Phys. Rev. E **77**, 036306 (2008).
 - [91] R. Marino, A. Pouquet, and D. Rosenberg, Phys. Rev. Lett. **114**, 114504 (2015).
 - [92] J. N. Reinhard, D. G. Dritschel, and C. K. Koudella, J. Fluid Mech. **474**, 175 (2003).
 - [93] C. Herbert, A. Pouquet, and R. Marino, J. Fluid Mech. **758**, 374 (2014).
 - [94] R. Marino, D. Rosenberg, C. Herbert, and A. Pouquet, EPL (Europhys. Lett.) **112**, 49001 (2015).
 - [95] P. C. di Leoni, P. J. Cobelli, P. D., and Mininni, Euro. Phys. J. E **38**, 1 (2015).